Experimental findings and SCAPS-1D simulations for high-efficiency MAPbI3 perovskite solar cells beyond 31%

Selma RABHI[a,b*], Karthick SEKAR[c], Karol KALNA[d], Yacoub Ibrahim BOUDERBALA[e], Nabil BOURI[f], Nouredine OUELDNA[g], Nacreddine BELBACHIR[h], Karima DADDA[a], Mohammed Saleh AIDA[k], Nadir ATTAF[l]

[a] Laboratory of Semi-conductors Material and Metallic Oxides, USTHB, Bab-Ezzouar,16111, Algeirs, Algeria.
[b] Dr. Yahia Fares University of Medea, Medea 26000, Algeria.
[c] University Limoges, CNRS, XLIM, UMR 7252, Limoges, F-87000, France.
[d] Nanoelectronics Devices Computational Group, Faculty of Science & Engineering, Swansea University, Swansea, SA1 8EN, United Kingdom.
[e] Applied Optics laboratory, IOPM, University of Ferhat Abbas, 19000, Setif 1, Algeria.
[f] Laboratory of Materials Physics and Subatomic, Faculty of Science, University Ibn Tofail, 14000 Kénitra, Morocco.
[g] Applied Chemistry and Engineering Research Centre of Excellence, Mohammed VI Polytechnic University, Ben Guerir 43150, Morocco.
[h] Department of Electrical Engineering, University of Abdelhamid Ibn Badis, 27000, Mostaganem, Algeria.
[k] Center of Nanotechnology, KAU University, Jeddah 22254, Saudi Arabia.
[l] University of Constantine, Street:BP 325, Route de Aïn-El-Bey, Constantine, Algeria.

Abstract

The sequence and texture of a methylammonium lead triiodide ($MAPbI_3$) phase deposited by a one-step spin-coating process are analyzed using X-ray diffraction, atomic force microscopy, profilometer, ultraviolet-visible spectroscopy to understand the film's fundamental properties. The structural results show that the formation of the $MAPbI_3$ crystalline phase adopts a tetragonal crystal structure. The optical results reveal a tetragonal crystal structure and a band gap of 1.53 eV, indicating its potential as an effective absorber of visible light. The *n-i-p* planar structure (ITO/SnO_2/$MAPbI_3$/Spiro-OMeTAD/Au) is then adopted for drift-diffusion SCAPS-1D simulations to optimise the performance of $MAPbI_3$ perovskite solar cells. The simulations finds that an optimal thickness between 2.3 μm and 4 μm, along with a defect density (Nt) of the $MAPbI_3$ absorber less or equal to 3×10^{13} cm^{-3}, improves the device efficiency from 22.55% to 23.17%. Additionally, the study explores the impact of different back and front contacts on solar cell performance, suggesting that RGO and AZO could effectively replace Au and ITO. The proposed solar cell structure (AZO/SnO2/$MAPbI_3$/Spiro-OMeTAD/RGO) demonstrates an impressive efficiency of 31.26%.

Keywords: $MAPbI_3$ perovskite, Solar cells, SCAPS-1D, Efficiency, Defects.

1. Introduction

From the first generation of single-crystal silicon solar cells to arising the third generations that include the dye-sensitized solar cells (DSSCs), organic solar cells (OSCs), quantum dot solar cells (QDSCs), and organic-inorganic hybrid perovskite solar cells (PSCs) have greatly attracted the researchers (Yuan et al., 2020; Zhang et al., 2015). Scientists have sought applications with outstanding power conversion efficiency (PCE), which is inexpensive to manufacture and has a minimal environmental impact during production and disposal. Among each of the various kinds of solar cells, PSCs and OSCs have gotten a lot of attention because they possess the ability to be extremely affordable and produced using low-energy methods (Hauck et al., 2017). Since 2009, quick progress in hybrid PSCs has taken its place in the photovoltaic (PV) industry. (Kojima et al., 2009). The efficiency of PSCs has increased significantly in a very short time, from 3.8% (Kojima et al., 2009) to 26% in 2023 (Zhao et al., 2022). Recently, KAUST set the highest world record on perovskite/silicon tandem monolithic, certified with a PCE of 33.7% (NREL, 2023), which is incomparable with the progress in Crystalline Silicon Solar Cells (SCs) (Lin H et al., 2023). PSCs have been attracted and considered as a promising alternative for SCs because of their interesting physical properties, such as a great absorption coefficient, a very high yield flexibility, a simple synthesis process at low temperatures (150-200 °C of thermal annealing is required at most), a high efficiency, an easy and a low cost of fabrication (Cheng and Lin, 2010; Kim et al., 2012; Liling et al., 2012; Takahashi et al., 2011). These advantages come from combining the properties of inorganic and organic materials, such as a direct band gap and a high absorption coefficient in the visible range (Eperon et al., 2014; Name and Kumar, 2014; Schulz et al., 2014). The most recommended organometallic lead halide elements in formulating the cell process in planar or mesoporous structures are methylammonium lead halides $CH_3NH_3PbX_3$/$MAPbX_3$ (Tidhar et al., 2014) and formamidinium lead halides $CH(NH_2)_2PbX_3$/$FAPbX_3$) (Im et al., 2012) (Heo et al., 2013). The component of methylammonium lead triiodide (i.e., $MAPbI_3$) is mostly used in PSCs because of its facility of elaboration compared with formamidinium lead triiodide ($FAPbI_3$). Kojima *et al.* (Kojima et al., 2009) initially utilized $MAPbI_3$ for solar cell *n-i-p* structure using a wet process, where the $MAPbI_3$ is the active/absorber layer (*i*), electron and hole transporter layers are *n* (ETL) and *p* (HTL), respectively.

Nevertheless, there are several ways to elaborate PSCs based on processing techniques, such as dry or wet processes, but the last one is particularly affordable and mostly used. (Isikgor et al., 2022; Khamkar et al., 2012; Nh et al., 2012; Zhou et al., 2014). A spin-coating deposition is a frequently used wet synthesis technique for depositing the $MAPbI_3$ thin films. This technique is primarily used through two main methods: the one-step and the two-step deposition approaches (Im et al., 2014). The one-step synthesis involves spin

coating a solution mixture of methyl ammonium iodine (CH_3NH_3I/MAI) and lead iodide (PbI_2), followed by annealing the films at 70 - 150 °C to crystallize them. On the other hand, the two-step process requires spin coating of the PbI_2 film first, then immersing it in a CH_3NH_3I solution, and promptly forming a $MAPbI_3$ layer upon rapid annealing. Although the two-step synthesis method facilitates the rapid fabrication of solar cells, its efficacy is hindered by the challenge of managing the rapid growth of $MAPbI_3$ in the solution (Burschka et al., 2013; Shaikh et al., 2017). In contrast, the one-step method holds an advantage in terms of cost-effectiveness and efficiency due to its simplified procedure, making it more favourable to larger-scale production. Therefore, the analysis of $MAPbI_3$ physical properties becomes instrumental in achieving optimal solar cell structures. The additional integration of a theoretical/simulation approach with this experimental work will accelerate and enhance this process.

To date, many studies have explored the PV behaviour of PSCs using a drift-diffusion SCAPS-1D software (Baloch et al., 2018; Hasnain, 2023; Karimi and Ghorashi, 2017; Karthick et al., 2020; Rahman et al., 2019). Whereas a majority of simulation studies concerning PSCs are conducted under ideal (non-real) conditions, relying only on theoretical physical characteristics, a few studies have used simulations under real conditions based on experimental data (Karthick et al., 2020). Moreover, the impact of the front contact on the overall performance of the PSC device is rarely studied. Therefore, this study addresses this gap by highlighting simulations conducted under real conditions, integrating experimental optical characteristics, such as the band gap and the thickness of the $MAPbI_3$ absorber. A systematic investigation and optimization of the absorber thickness and defect density (N_t) was conducted. The optimum absorber thickness was found between 2.3 μm and 4 μm, and the N_t should be less than or equal to 3×10^{13} cm^{-3}. Finally, we demonstrate the effect of different rear and front contacts on the solar cell performance. The results confirm that using AZO and RGO instead of ITO and Au in a solar cell structure (i.e., AZO/SnO_2/$MAPbI_3$/Spiro-OMeTAD/RGO) provides a higher efficiency of 31.26%.

2. Experimental details and methods

2.1. Materials

Methylamine (40 wt% in methanol, Sigma Aldrich), hydroiodic acid (HI, 57 wt% water, Avantor VWR), lead iodide (PbI_2) (99%, Sigma Aldrich), N-N dimethylformamide (DMF, anhydrous, 99.8%, Sigma Aldrich), diethyl ether (DEE, ≥99.5%, GC, Sigma Aldrich), isopropanol (IPA, anhydrous, 99.5%, Sigma Aldrich), acetone and ethanol (99%, Sigma Aldrich) were used as received without any further purification.

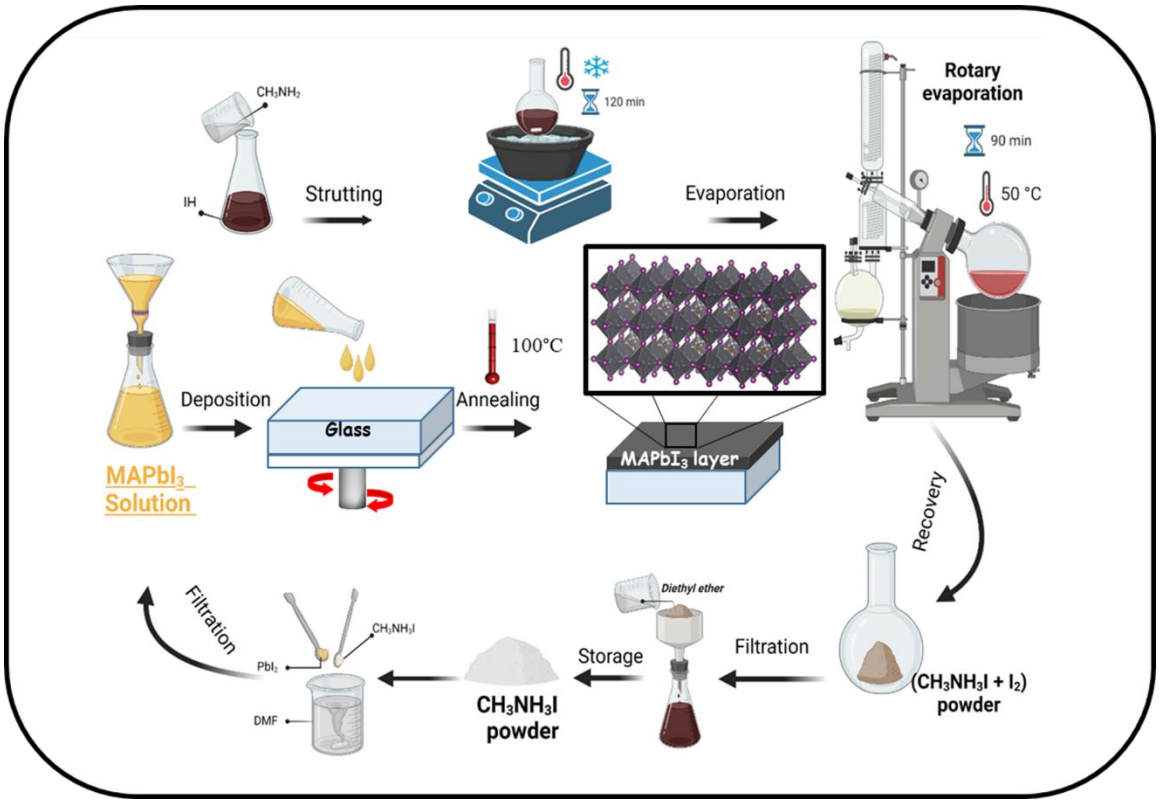

Fig. 1. Illustration of the perovskite layer fabrication: a synthesis of the perovskite precursor solution and a deposition process of the perovskite layer out of glove box.

The samples are deposited on glass substrates (76 x 26 x 2 mm, Naturoptic), using 0.45 µm diameter filters (Nylon syringe filters, Aijiren).

2.2. Material Synthesis and film fabrications

In this study, a thin layer of $MAPbI_3$ was deposited on a glass substrate using the one-step spin coating technique. **Fig. 1.** summarized the $MAPbI_3$ powder synthesis and film deposition process. The preparation of $MAPbI_3$ films was achieved in three steps: (1) MAI powder was prepared by vacuum distillation using evaporator equipment at 50 °C for 1h, which eliminates the solvent by means of low pressure. Whereas the evaporating of a mixing solution made of 27.8 mL of methylamine (40 wt% in methanol) with 30 mL of hydroiodic acid (57 wt% water) after agitation in a flask in an ice bath (0 °C) for 2 h. The purpose of using an ice bath is to avoid any reaction between compounds. The obtained powder was washed with diethyl ether several times to eliminate the residual of non-bound iodine. We measured its melting temperature using Kofler-bench equipment to confirm the complete presence of MAI. The melting temperature of the commercial powder measured was between 260 °C and 280 °C, whereas the temperature measured by the Kofler-bench was around 270 °C, showing that the powder obtained was indeed MAI.(2) The $MAPbI_3$

solution was prepared by mixing 0.563g of MAI and 1.6551g of PbI_2 within 2.873 ml N, N-dimethyl formamide (DMF). The obtained yellow solution was purged with a flux of nitrogen to eliminate oxygen and filtered through 0.45 µm diameter filters to remove the precipitates produced, and then the final product was stored in a dark box. (3) $MAPbI_3$ deposition: films were deposited on cleaned glass substrates (76 x 26 x 2 mm) placed on the support of the spin coating device and with a rotation speed of 500 rpm for 9 seconds, then 1000 rpm for 30 seconds, finally, 2500 rpm for 30 seconds. Then, annealing at a low temperature of 100 °C for 15 minutes was required to achieve stable, black-colored perovskite phase.

2.2 Characterizations

Grazing incidence X-ray diffraction (GIXRD) measurements were carried out using a Philips X' Pert diffractometer with Cu Kα radiation (λ = 1.5418 Å) to carrier out an *ex-situ* measurement for this sample from 10° to 60° at room temperature. UV-visible absorption spectra were recorded on a Shimadzu UV-3101PC UV-Vis-NIR Spectrophotometer. A profilometer ALTISURF®500 was used to measure the thickness of the layer deposited on a substrate. In order to investigate the morphology of the sample, PHYWE Atomic Force Microscopy (AFM) was used.

3. Numerical simulation of devices using SCAPS-1D

In this study, the simulations are carried out using the Solar Cell Capacitance Simulator SCAPS-1D, version 3.3.10 (Burgelman et al., 2000). The SCAPS-1D simulations allow us to discuss the influence of perovskite absorber thickness and other solar cell layers under different conditions (i.e., ideal and real conditions) on PV parameters. Moreover, varying input parameters, including relative permittivity, band gap, thickness, doping concentration, and bulk charge carrier density of any solar cell layer (ETL, absorber, HTL), will significantly influence the device's PV performance. The SCAPS-1D simulations are carried out to reduce the cost of real tests and quickly find suitable experimental parameters. The simulation method is based on a classical drift-diffusion model and solve the electron and hole continuity equations and Poisson's equation (Burgelman et al., 2000). And. To this aim, a 1D planar semi-transparent PSCs *n-i-p* type structure is modelled and simulated by SCAPS-1D because of its performance and simplicity. The PV parameters of the PSCs, such as open circuit voltage (V_{oc}), short-circuit current density (J_{sc}), fill factor (FF), and power conversion efficiency (PCE), are recorded to understand the solar cell performance.

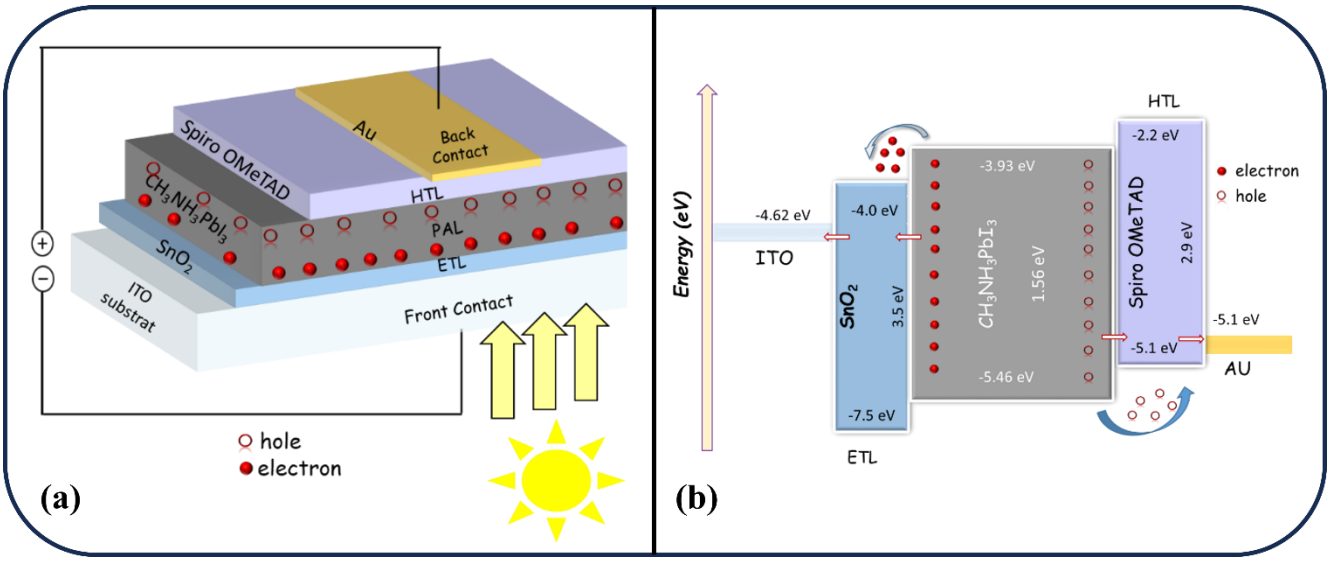

Fig. 2 a) Schematic of design of PSC *n-i-p* structure used in this SCAPS simulation (i.e., ITO/SnO_2/$MAPbI_3$/Spiro OMeTED/Au), with layer thicknesses of 130 nm, 2.92 µm and 350 nm for ETL, PAL and HTL, respectively. B) Schematic energy level diagram of different materials used in the PSC.

Here, the chosen semi-transparent PSC device consists of indium-doped tin oxide (ITO) as the transparent conductive oxide (TCO), tin oxide (SnO_2) as ETL, $MAPbI_3$ as a Perovskite Absorber Layer (PAL), 2,29,7,79-tetrakis-(N, N-di-p-methoxy phenylamine) 9,99-spiro bi-fluorene (spiro-OMeTAD) as a P-type HTL, and Au representing the back metal contact (simply ITO/SnO_2/$MAPbI_3$/spiro-OMeTAD/Au), shown in **Fig. 2a**, respectively. The performance of solar cells is influenced by the alignment of energy levels, which plays a very important role because when an ETL or/and HTL material whose energy levels are aligned with those of the perovskite, charges can be easily transferred from the PAL to the interface layers (Schulz et al., 2019). So the band conduction (BC) of the ETL must be low compared with that of the PAL, and likewise, the valence conduction (VC) of the HTL should be a little higher than that of the PAL to extract electrons and holes effectively (Calió et al., 2016; Serhan et al., 2019). In addition, both electrodes should facilitate better charge transfer from adjacent layers, and their work functions should match the energy levels of adjacent layers (Serhan et al., 2019). Therefore, the materials we have chosen as layers for this cell are suitable for the energy alignment conditions, as shown in **Fig. 2 b**. The principle of operation of PSC I in the ideal case is as follows: Sunlight passes through the ITO and is absorbed by the PAL, creating electron-hole pairs. The electrons then move towards the SnO_2 ETL, initiating a primary charge separation, while the holes move towards the Spiro OMeTED HTL, creating a potential difference that generates an electric current. However, in the real case, energy dissipation from the recombination process lowers efficiency. In general, recombination processes happen through radiative, Auger, and Shockley-Read-Hall (SRH) (known as non-

radiative recombination) mechanisms. Leijtens et al. reported that in PSCs, non-radiative recombination has a stronger influence, significantly affecting the PSC performance, and limiting the efficiency compared to radiative recombination (Leijtens et al., 2016). The simulations are carried out at 300 K under one sun irradiation with integrated power density 1000 W m^{-2} (AM1.5G) according to standard solar cell test conditions (Dunlop et al., 2010). The optical band gap of the PAL and its thickness are obtained from the experimental transmittance spectra and mechanical UV spectrum measurements. All the input parameters used in the simulations are listed in **Table S1.** The PAL, ETL and HTL physical input parameters, such as thickness, bandgap, electron affinity, permittivity, effective density of states, charge mobility, thermal velocity, doping and defect density were extracted from the literature (Hao et al., 2014; Hossain et al., 2023; Kemp et al., 2013; Nakka et al., 2022; Rutledge and Helmy, 2013). The simulation study is divided into two sections: (i) ideal and (ii) real conditions. The ideal conditions which neglect defects, band-to-band recombination and resistance, provide valuable information on the fundamental characteristics and properties of the material used in the PSC and serve as a handy tool for estimating the device's maximal theoretical performance when evaluating its ideal functioning. The real conditions reflect the challenges and conditions at which solar cells will encounter in practical applications (actual devices). This assessment is crucial in determining the technology's potential for scale-up and commercial viability. Comparing the solar cell PV performance under ideal and real conditions enables researchers to identify and quantify the various loss mechanisms that limit efficiency in the real world. Therefore, the realistic condition-based SCAPS-1D simulation study guides the solar cell design and aims to understand and reduce these mentioned recombination losses and improve the overall device efficiency.

4. Results and discussion

4.1 Structural and Topographical analysis

At room temperature, an ex-situ XRD pattern with a wavelength λ of 1.54 Å were carried out and presented in **Fig. 3**. The diffraction peaks at 14.00°, 20°, 23.57°, 24.40°, 28.27°, 31.79, 34.95°, 40.58°, and 42.98° correspond to (110), (200), (211), (202), (220), (310), (312), (224), and (314), respectively, of a tetragonal perovskite structure as reported in literature (Dang et al., 2016; Lee et al., 2012; Loi and Hummelen, 2013). The most intense diffraction peaks at 14.00° and 28.27° of (110) and (220), indicate a highly oriented crystal structure and enhanced crystallinity. The presence of a small signature at the highest peak of the $MAPbI_3$ phase, the peak at 12.60°, corresponds to the (001) diffraction peak for PbI_2. The peak reveals that the $MAPbI_3$ phase deposited has a high level of phase purity (Liang et al., 2015). Using Bragg's law:

$$2d \sin\theta = n\lambda \ldots\ldots\ldots\ldots (1)$$

and the relation between the interplanar distance d and Miller indices (hkl):

$$d_{hkl} = \frac{a}{\sqrt{h^2+k^2+l^2(\frac{a}{c})^2}} \ldots\ldots\ldots\ldots\ldots\ldots (2)$$

we could determine the lattice parameters of $MAPbI_3$ where: a = 8.912 Å and c = 12.604 Å.

From the XRD pattern and using the most intense diffraction peaks, we calculated the average D of crystallite sizes and the strain ε in films by the Scherrer and Williamson–Hall methods (Rousseau and Gibaud, 2006):

$$D = \frac{0.9\lambda}{FHWM\ cos\theta} \ldots\ldots\ldots\ldots\ldots\ldots (3)$$

$$FHWM\ cos\theta = \frac{\lambda}{D} + \varepsilon\ sin\theta \ldots\ldots\ldots (4)$$

$$FHWM\ cos\theta = \frac{\lambda}{D} + \varepsilon\ sin\theta \ldots\ldots\ldots (5)$$

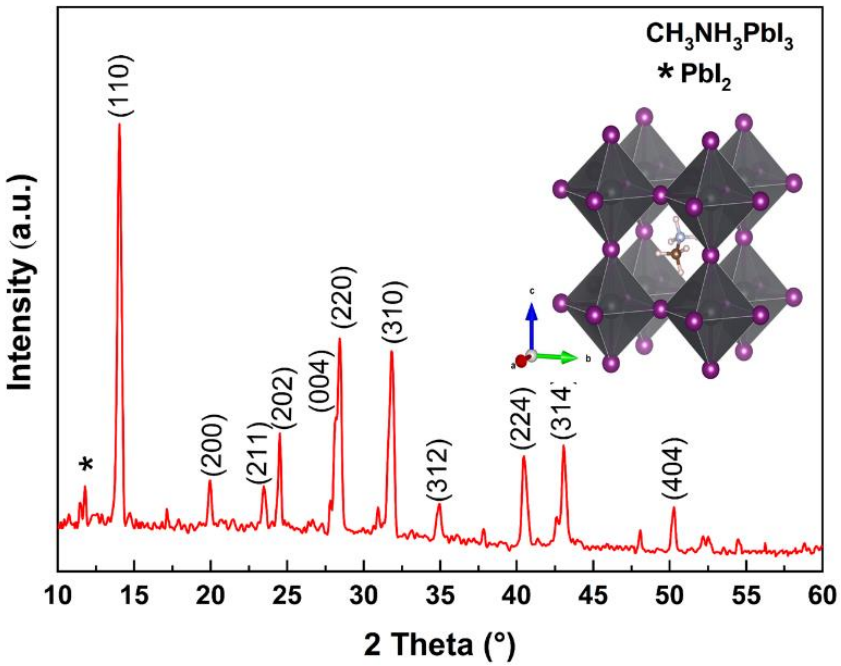

Fig. 3. XRD patterns of the $MAPbI_3$ film deposited on glass. Inset: a crystal structure of $MAPbI_3$.

In the case of polycrystalline thin films, certain crystalline orientations are not detectable using (Burgelman et al., 2000), as only grains whose planes are parallel to the substrate are observed. The obtained results show that crystallites with an average crystallite size of 50 nm are subject to a low deformation of the order of 0.14%. This may be related to the choice of a high spinning speed (2500 rpm), where the crystallite size and strain are reduced with increasing spinning speed (Belaidi et al., 2019). Although these grain sizes are

much smaller than the typical range seen in high-performance $MAPbI_3$ solar cells, which is around 100-500 nm, this size is recommended because the larger average grain size forces fracturing occur along the interface between $MAPbI_3$ and other layers in the solar cell (Dai et al., 2020).

In addition, a 3D AFM image of the sample is presented in **Fig. S1**. The deposited layer shows continuously and is free of porosity, which means that another layer could be deposited on top, such as the spiro-MeOTAD HTL or SnO_2 ETL. However, the deposited layer is not homogeneous and uniform, and it has an average roughness (R_a) of over 41 nm, for a thickness of 2.92 ± 0.005 μm measured by a profilometer. Even with this thickness of $MAPbI_3$, the roughness is much higher than the typical range of roughness observed in high-performance $MAPbI_3$ solar cells (Yang et al., 2022). Therefore, adjusting the spinning speed and the concentration of DMF might help to improve the absorber layer, decreasing the roughness and thickness.

4.2 Optical analysis

Fig. 4. a shows the transmittance (T%) spectra of $MAPbI_3$ film deposited on glass from the ultraviolet (UV) range to the near-infrared (NIR) range. We observed that the transmittance of $MAPbI_3$ does not exceed 35% in the visible range, indicating its high absorption. We also remarked in the transmittance spectra two absorption edges. One in the UV range, located at about 300 nm, comes from the absorption characteristics of the glass substrate used to deposit the $MAPbI_3$ layer. On the other hand, a second front is nearly located at about 750 nm, in the long wavelength region (at the NIR range), corresponding to the optical absorption of the perovskite film. These particular edges and the allure of the absorption curve were used to estimate the band gap of the film, whereas the absorption curve was calculated from transmittance spectra based on Beer-Lamber law's:

$$T = e^{-\alpha} d \ldots\ldots\ldots\ldots (6)$$

Moreover, the bandgap E_G was estimated by using the Tauc relation:

$$\alpha h\nu = A[h\nu - E_G]^n \ldots\ldots\ldots\ldots (7)$$

where d is the thickness of $MAPbI_3$ film (2.92μm), *A* is a constant, and *n* was taken as equal to 1/2.

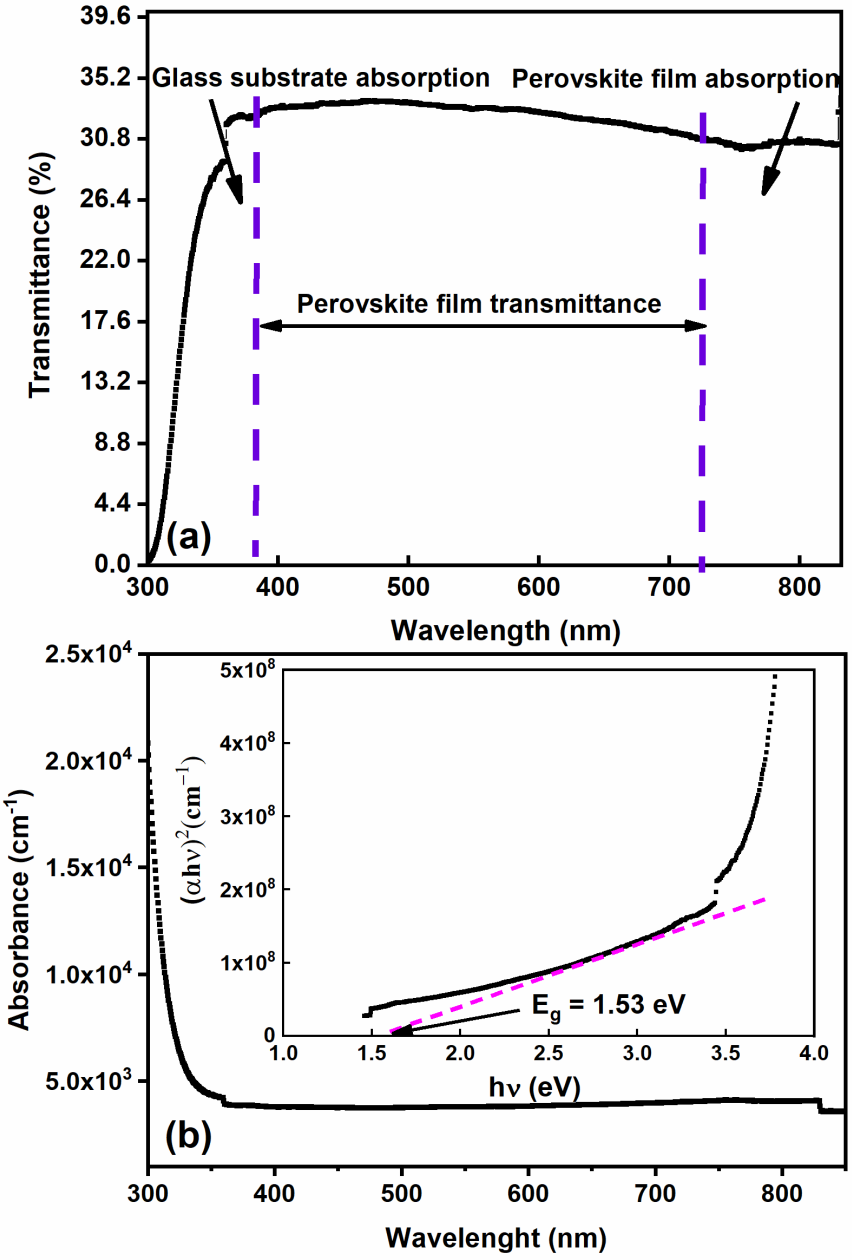

Fig. 4. (a) UV–visible transmission and (b) the absorbance spectra of $MAPbI_3$ film. The inset shows the corresponding Tauc plot used for bandgap calculations.

Fig. 4. b shows the absorption $f(\lambda)=\alpha$ plot. As in the transmittance spectra, we observe that there is a strong fundamental absorption from 360 nm to ~ 830 nm, where the transmittance is low, indicating a significant absorption in the visible range, as mentioned before, with an absorption coefficient α around 5×10^3 cm^{-1}. Moreover, the deposited PAL is almost black (grey-dark), which means it presents a high absorption. This allows us to estimate a bandgap of 1.53 eV, as shown in the inset in **Fig. 4.**, which presents the plot of the curve of $(\alpha h\nu)^2 = f(h\nu)$. Hence, the absorbance and the transmittance spectrum demonstrate that this is a

semiconductor with a direct bandgap of 1.53 eV and a strong UV absorption. Moreover, this absorption characteristic is consistent with the optoelectronic properties of $MAPbI_3$. These values were used in the SCAPS-1D simulations of the PSC solar cell.

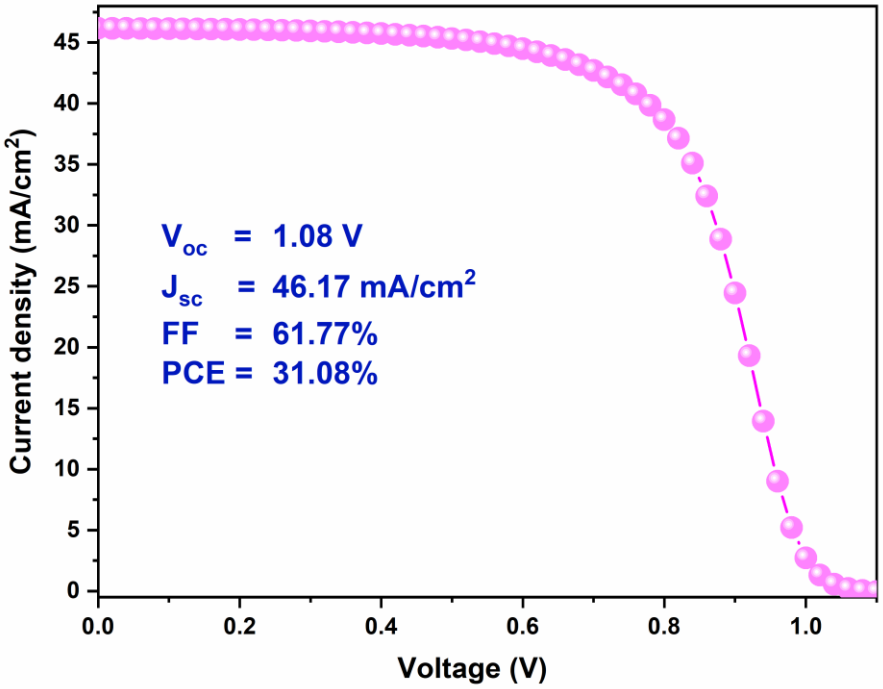

Fig. 5. J-V characteristics of the $MAPbI_3$-based solar cell with the photovoltaic parameters.

4.3 Model and Simulations

4.3.1 Ideal conditions

The ideal device's current-voltage characteristics (J-V) curve is presented in **Fig. 5.** with the corresponding PV parameters. The overall current density for the configuration is calculated to be $J_{SC} \cong 46.2$ mA/cm^2 at V_{OC} of $\cong$ 1 V, which yields an FF of $\cong$ 62% with PCE of $\cong$ 31.1 %. Considering the reported $MAPbI_3$ properties, these results are assumed to represent the practical limit, neglecting defects and band-to-band recombination. The results are very close to the reported maximum PCE limit of around 31% for a $MAPbI_3$-based PSC (Sha et al., 2015). More importantly, the obtained results under ideal conditions serve as an essential reference point and establish the material's potential that we chose for this PSC structure. A study the performance of PSC under real conditions requires considering a band-to-band recombination reflection and a contact resistance.

4.3.2 Real conditions

Herein, we investigate the impact of defects and a band-to-band recombination on the solar cell performance in practical applications considering resistances and reflectance. **Table S2** shows the recombination process parameters of the customized PSCs (Baloch et al., 2018; Ford et al., 1997; Zandi and Razaghi, 2019). In the following, the real condition is considered to have two distinct stages, starting with radiative and then Auger recombination. The application of radiative recombination coefficients to the solar cell's ETL, PAL and HTL has a remarkable influence on the device performance. This real simulation predicts V_{OC} = 1 V, J_{SC} = 46.15 mA/cm^2, FF = 56.76%, and PCE = 26.14% for the PV parameters of this solar cell, a dramatically decrease. On the other hand, the effect of Auger recombination is almost negligible, the predicted PV parameters (V_{OC} = 0.96 V, J_{SC} = 46.15 mA/cm^2, FF = 56.57%, and PCE = 25.18%) decreased marginally. Compared with the Auger recombination, the radiative recombination is the dominant mechanism in PSCs due to their direct bandgap and large dielectric constant, which means a photon emission is very efficient via band-to-band transitions (Hosseini et al., 2022).

However, resistance and reflectance also play a role in addition to the band-to-band recombination. Highly efficient devices R_{series} must be less than 1 Ω.cm^2 and R_{shunt} greater than 10^7 Ω.cm^2 (Abderrezek, 2015). Overall, the fundamental origin of the R_{series} is the impedance of the electrodes: front and rear contacts (ITO and Au), but the R_{shunt} effect is due to manufacturing defects. Therefore, in order to comprehend how parasitic resistances (R_{series} and R_{shunt}) affect the performance of PSC, which dissipates the power produced by the solar cell in the form of electrical losses, we introduced them in the SCAPS-1D model, whereas R_{series} = 1 Ω.cm^2 and R_{shunt} = 10^7 Ω.cm^2 are applied consequently. Herein, obtained FF and PCE dropped from 56.57% to 53% and 25.18% to 23.57%, respectively, where the V_{OC} and J_{SC} remained constant. R_{series} affects FF, resulting in a global PCE reduction due to a higher power loss. Otherwise, a high R_{shunt} lowers the p/n junction resistance and impacts the amount of collected photocurrent, allowing more current to flow through it and increasing the solar cell performance. In addition to resistance, the reflection was applied in the last step, especially the reflection value of the ITO contact is adjusted by 5% (Sibin et al., 2016). This adjustment is significant because approximately 95% of the incident light can penetrate or transmit through the ITO substrate, making it suitable as front contact in solar cells, which will not affect the solar cell's performance highly. Whereas the results were acquired as V_{OC} = 0.96 V, J_{SC} = 43.83 mA/cm^2, FF = 53 %, and PCE = 22.55%. However, applying reflection impacts the PSC, where the J_{SC} is reduced from 46.15 mA/cm^2 to

43.83 mA/cm^2 and reduced by 1% PCE (see **Fig.6**). This impact is not large compared with the effects of R_{series} and R_{shunt}.

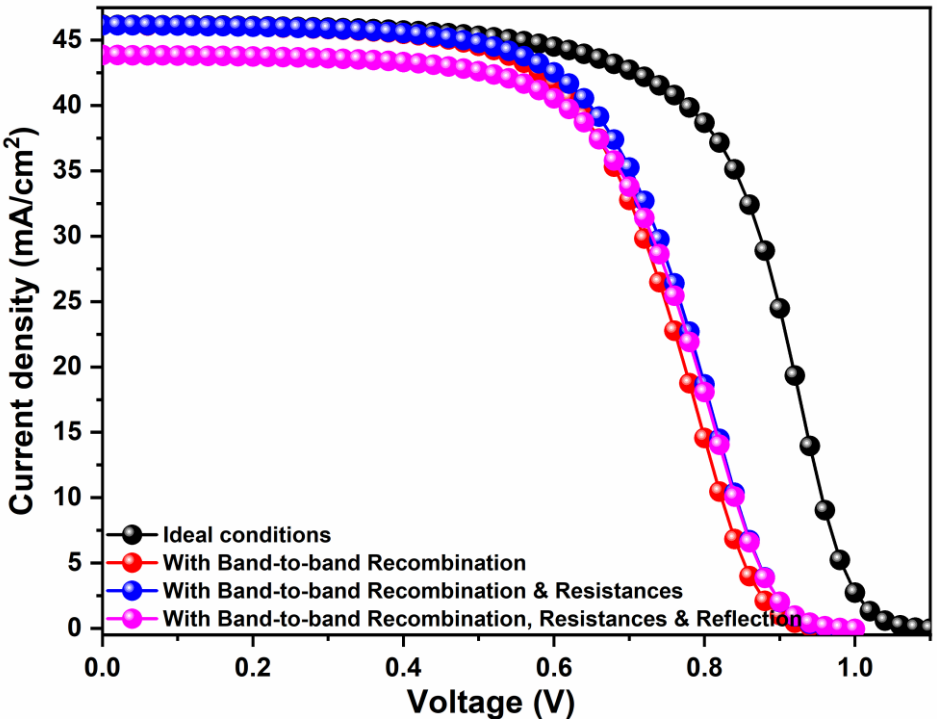

Fig. 6. Comparison of the ideal and realistic conditions J-V characteristics.

The simulated J-V curves of the previous phases are shown overlapping in **Fig. 6**. As the simulations assimilated more real conditions, the device performance gradually decreased, revealing a more realistic performance level. The corresponding evolutions of the main photovoltaic parameters are collected in ***Table 1***.

Table 1. Photovoltaic parameters of PSCs under different ideal and real conditions.

Simulation parameters	V_{OC} (V)	J_{SC} (mA/cm^2)	FF (%)	PCE (%)
Ideal conditions	1.10	46.20	63.00	31.10
Applying band-to-band recombination, resistances, and reflection	0.96	43.83	53.35	22.55

4.3.3 Influence of PAL Thickness and Defect Density on PV Performances

In PSCs, the thickness of the PAL significantly affects the PV parameters as it plays a crucial role in light absorption and charge generation. The PCE is one of the factors most susceptible to responding consistently

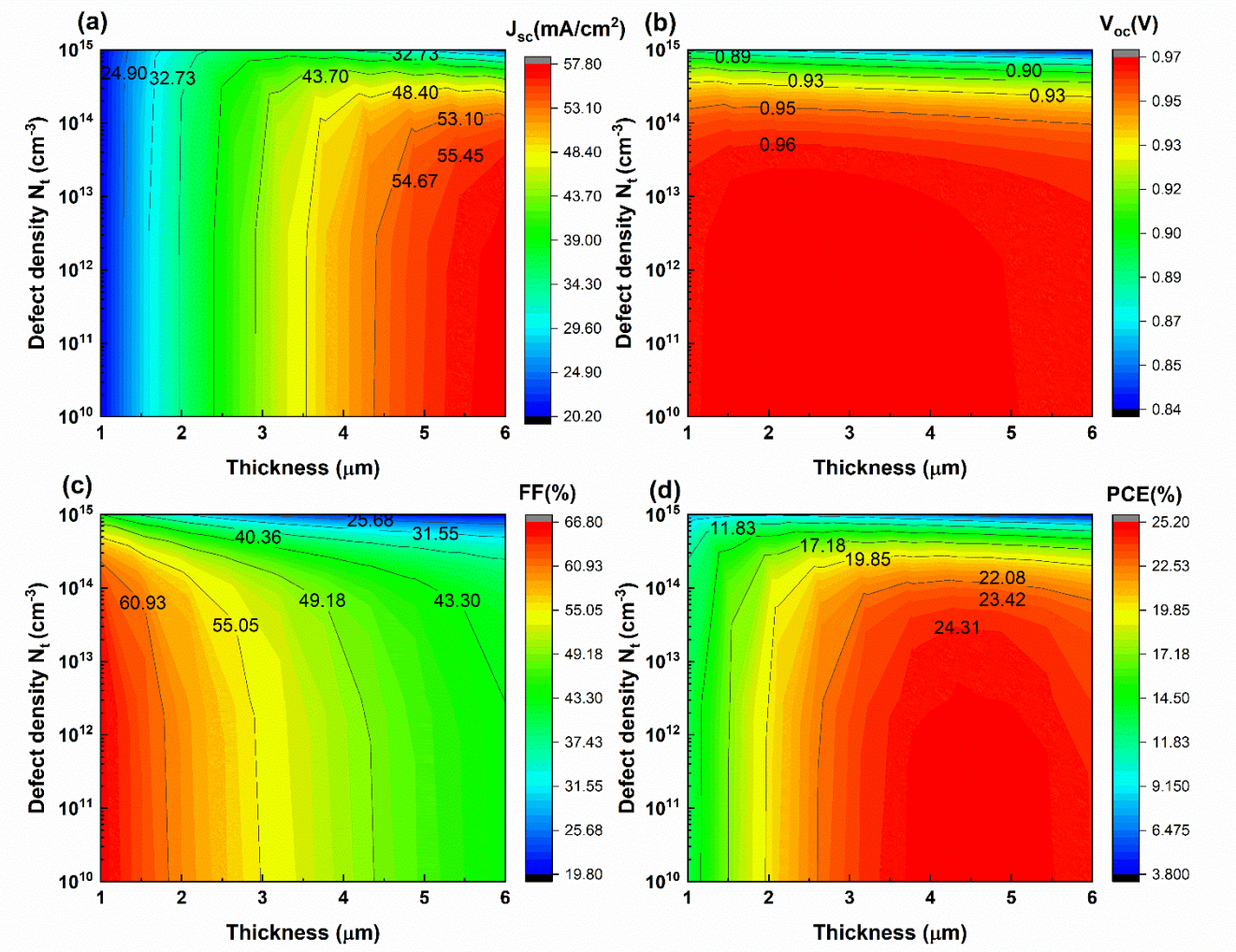

Fig. 7. Contour mapping of the PSCs performance showing a short-circuit current density, J_{SC} (a), an open circuit voltage, V_{OC} (b), a fill factor, FF (c), and a power conversion efficiency, PCE (d) with a variation of the thickness and N_t of the PAL.

to the degree of variation in input parameters, as well as manufacturing defects significantly affecting the PV performance of PSC. In order to achieve a better performance, an optimum thickness and defect density (N_t) of the PAL is crucial. The contour maps of the projected V_{OC}, J_{SC}, FF, and PCE with respect to the varying absorber thickness (1μm to 6 μm) and N_t (1×10^{10} cm^{-3} to 1×10^{15} cm^{-3}) for the $MAPbI_3$-based PSCs are shown in **Fig. 7**. These contour maps illustrate how the PV parameters are affected by the combined change of absorber N_t and thickness. In **Fig. 7a,** the J_{SC} extended to a maximum value of 57.8 mA/cm^2 when the N_t was around > 3×10^3 cm^{-3} and PAL thickness was > 4 μm. Similarly, in **Fig. 7b**, the V_{OC} remains relatively constant when the thickness increases and $N_t < 3\times10^{13}$ cm^{-3}. When $N_t > 3\times10^{13}$ cm^{-3}, V_{OC} drops slightly from 0.960 V to 0.893 V, which means that the presence of defects is

mainly responsible for the observed change in V_{OC} for the conventionally structured solar cell. On the other hand, FF decreases progressively from 66.8% to 19.80% because FF is inversely proportional to the thickness, N_t, as shown in **Fig. 7c** . Furthermore, **Fig. 7d** shows that when $N_t < 3 \times 10^3$ and PAL thickness ≤ 3 μm, the highest PCE value of 25.20% was achieved.

In order to extract the optimum conditions and to clearly visualize the effect of the thickness and N_t in the PAL, the performance of the PSCs is plotted as a function of the thickness and N_t, as shown in **Fig. S2a** and **b,** respectively. **Fig. S2a** shows that V_{OC} remains constant with the rise of thickness (a variation is between 0.960 V and 0.965 V, which is negligible). V_{OC} is mainly related to the materials used rather than the thickness of the PAL and the interfacial accumulation of charge carriers (Daboczi et al., 2019). Meanwhile, J_{sc} increases steadily with thickness, which is explained by the heightened light absorption in the thicker PAL, leading to an enhanced current generation (Pochont and Sekhar, 2023). Contrarywise, FF presents a gradual decrease with the increased thickness due to the possibility of an increase in the series resistance in thicker devices, leading to a reduction in FF (Shyma and Sellappan, 2022). PCE initially increases with the thickness and reaches its maximum PCE at a thickness of 4 μm. This could be justified by the fact that there is a linear relationship between the increase in the thickness and the absorption of light, leading to the generation of a greater number of electron-hole pairs, i.e., increasing the photocurrent and thus improving the efficiency of energy conversion. Then, the PCE starts to decrease from 23.96% to 22.80%, which is often related to the diffusion length of charge carriers within the material. The charge carrier recombination becomes more prominent, leading to decreased efficiency by affecting the FF and V_{OC} and increasing J_{SC} (which increases the light absorption) when the thickness of the PAL exceeds the critical diffusion length of charge carriers (Deepthi Jayan and Sebastian, 2021). Therefore, **Fig. S2a b** demonstrates that all PV parameters declined as the absorber N_t was increased from 3×10^{12} cm^{-3} to 10^{15} cm^{-3}. Consequently, optimizing the PAL thickness and N_t for best performance by maximizing light absorption and minimizing recombination losses is vital. The results show that a thickness of 2.3 μm to 4 μm and N_t less than 3×10^{13} cm^{-3} offer a high performance. However, The obtained PV parameters are V_{OC} = 0.966 V, J_{SC} = 43.89 mA/cm^2, FF = 54.65%, and PCE = 23.17%. Therefore, after optimization, the chosen optimum thickness is fixed at 2.92 μm, and the optimization parameters will be included in the next performance evaluation stage to find suitable front and back contact materials.

4.3.4 *Impact of the work function of front and back contact on PV performances*

There are several studies (Deepthi Jayan and Sebastian, 2021; Hossain et al., 2023; Makableh et al., 2020) where the back metal work function (WF) has been varied to get better performance, but so far, no studies have reported the effect of WF on front contact. Herein, we reported the impact of the WF of both contacts (front and back) on the PSCs performances for the first time. **Table S3** summarizes the WFs of various materials for the back and the front contact, such as silver/argent (Ag), copper (Cu), iron (Fe), gold (Au), nickel (Ni), reduced graphene oxide (RGO), selenium (Se), Al-doped zinc oxide (AZO), F-doped tin oxide (FTO), and indium tin oxide (ITO) extracted from literature (Garg et al., 2014; Hossain et al., 2023; Joo et al., 2021; Qasim et al., 2022; Reyes et al., 2021).

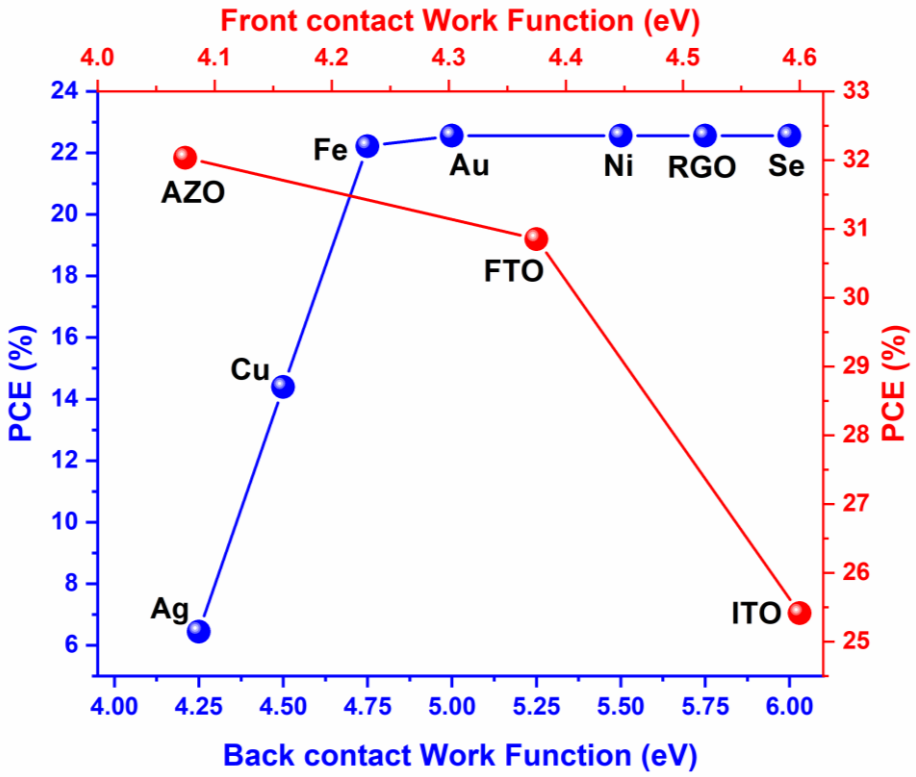

Fig. 8. The effect of work function (WF) of different contacts (the back and the front contacts) on the PCE of planar PSCs.

The PCE of our simulated solar cell with varying back contact is shown in **Fig. 8**. The increasing WF of metals up to a value of ~ 4.75 eV increases the PSC performance, then saturates at 5.0 eV. This could be attributed to the $MAPbI_3$ WF (-5.46 eV), which saturates the efficiency due to the alignment of the HTL WF and the valence band of the absorber layer. With the use of a high metal WF, the Fermi level energy decreases

due to the band bending at the metal-semiconductor interface, which makes the contact more ohmic and the type of contact we attempt to achieve in PSC (Behrouznejad et al., 2016).

Fig. 8. demonstrates that the Au, Ni, Se, and RGO electrodes offer a similar and higher PCE compared to the Ag and Cu electrodes. As a result, we have chosen the RGO instead of back contacts due to its low cost, high conductivity and emissivity, and good stability (Makableh et al., 2020; Zhang et al., 2021). Similarly, for the front contact (see **Fig. 8**.), the PCE is unchanged until a WF value of 4.38 eV, then it decreases to a higher WF value of 4.6 eV (i.e., the WF value of ITO). The efficiency reduction from 31.2% to 25.4% could be explained by a front contact with a high WF leading to increasing the interface recombination as an energy barrier prevents electron transfer into the front contact and the occurrence of inverted band bending, which hinders charge transport and collection. Usually, to achieve an optimal PSC performance, choosing a front contact with a WF slightly higher than the conduction band of PAL ($MAPbI_3$, ~ 4.0 eV) is crucial, which has a dominant impact on the solar cell performance.

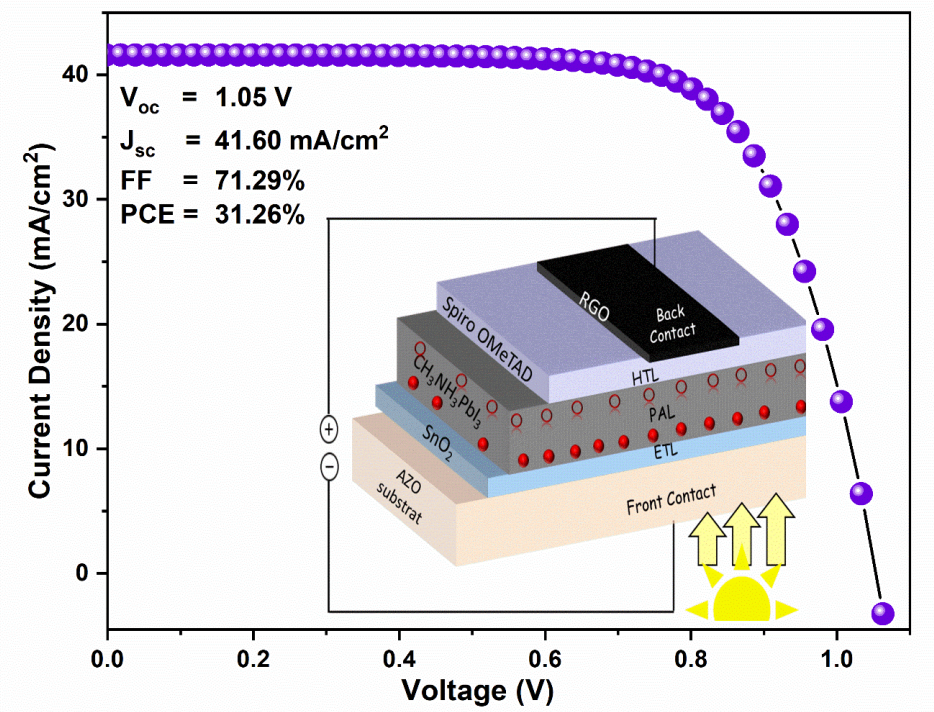

Fig. 9. J-V characteristic of the $MAPbI_3$-based solar cell with the PV parameter. The inset shows a new schematic design of *n-i-p* structure for PSC (AZO/SnO_2/$MAPbI_3$/Spiro OMeTED/RGO).

Therefore, after all these optimizations, we have chosen the RGO (WF of 5.72 eV) and AZO (WF of 4.19 eV), which could be effective alternatives to replace Au and ITO. Using the optimum values of thickness and N_t

and keeping the same real conditions, except the AZO transmittance (here is taken 90%), the proposed device structure of AZO/SnO_2/$MAPbI_3$/Spiro OMeTED/RGO delivers an excellent efficiency of 31.26% with the corresponding PV parameters of J_{sc} = 41.60 mA/cm^2, V_{oc} = 1.05 V, and FF = 71.29%. The relevant J-V characteristics plot is displayed in **Fig. 9,** and importantly, the obtained PCE (31.26%) is closer to the Shockley-Queisser limit (i.e., 33%) (Shockley and Queisser, 1961). Jiang et al. investigated the thermalization study for nine different PSC structures using various front (ITO, FTO, AZO) and back contacts (Au, Ag, RGO) using the COMSOL Multiphysics commercial package (Jiang et al., 2022). Their results exhibit that the PSC containing AZO and RGO as the front and the back contacts reduced the maximum operating temperature to 31.1 °C. Whereas, with other contacts such as Au and ITO, the operation temperature could achieve 70°C, which reduces the performance of PSCs.

Table 2 summarizes experimental and theoretical works on PSCs employing AZO and RGO as the front and the back contacts. Recently, W. Wang *et al.* experimental studies showed that the PSCs with a textured AZO front contact device structure (**AZO**/SnO_2/$MAPbI_3$/Spiro OMeTAD/Au) offer an excellent PCE of ~ 18% (Wang et al., 2023). Their results explain that the AZO-containing device efficiently suppresses the charge recombination and decreases the energy barrier at the AZO/ETL interface, which smooths electron extraction and, as a result, enhances the PV performance. In addition, S. Rawat *et al.* drift-diffusion SCAPS-1D investigations using the AZO front contact with $MASnPbI_3$ PAL-based PSCs offered PCE of 26% and 28% (Rawat et al., 2023). Similarly, C. Zhang *et al.* experimental findings proved that the RGO back contact-based PSCs (FTO/SnO_2/perovskite/spiro-OMeTAD (HTL)/**RGO**) with and without HTL provide a good efficiency of 16.8% and 12.6%, respectively (Zhang et al., 2021). Furthermore, their results also confirm that the titanium-doped RGO (Ti-RGO) electrode-based PSCs further enhance the PCE from ~ 17% to ~ 20%. Likewise, the RGO‑MoS_2 nanocomposite and GO top electrode-based simulated PSCs (ITO/CuSCN/$MAPbI_3$/PCBM/RGO-MoS_2 and FTO/SnO_2/Cs_2PtI_6/MoO_3/GO) provide ~ 20% and ~ 22% of efficiency (Amjad et al., 2023; Safie et al., 2022). This present work, especially a proposed novel device design (AZO/SnO_2/$MAPbI_3$/Spiro OMeTED/RGO), delivers the highest PCE of 31.2% compared to the published reports (Amjad et al., 2023; Dou et al., 2017; La Ferrara et al., 2017; Rawat et al., 2023a; Safie et al., 2022; Sekar et al., 2022; Zhang et al., 2021).

Table 2. Summary of the $MAPbI_3$ PSCs reported in the literature.

Device structure	Jsc (mA/cm^2)	Voc (V)	FF (%)	PCE (%)		Ref
AZO/$MASnPbI_3$/NiO	35.93	0.90	87.13	26.17	Sim	(Rawat et al., 2023)
AZO/ZnONWs/$FACsPbIBr_3$/ Spiro OMeTAD/Au	16.10	0.64	47.00	04.90	Exp	(Sekar et al., 2022)
AZO/ZnONRs/$MAPbI_3$/Spiro OMeTAD/Au	16.00	0.80	53.00	07.00	Exp	(La Ferrara et al., 2017)
AZO/SnO_2/FAMACs/Spiro OMeTAD/MoO_3/Al	21.99	0.99	55.70	12.20	Exp	(Dou et al., 2017)
AZO/SnO_2/FAMACs/Spiro OMeTAD/Au	19.40	1.10	69.90	15.00	Exp	(Barbé et al., 2019)
AZO/SnO_2/$MAPbI_3$/Spiro OMeTAD/Au	23.70	1.04	70.00	17.60	Exp	(Wang et al., 2023)
AZO/$MASnPbI_3$/NiO	35.93	0.96	78.97	27.94	Sim	(Rawat et al., 2023)
FTO/SnO_2/perovskite/spiro-OMeTAD/**RGO**	22.10	1.10	69.00	16.80	Exp	(Zhang et al., 2021)
FTO/SnO_2/perovskite/**RGO**	24.00	0.99	52.20	12.60		
ITO/CuSCN/$MAPbI_3$/PCBM/ **RGO** with MoS_2	25.26	1.16	67.15	19.68	Sim	(Safie et al., 2022)
FTO/SnO_2/Cs_2PtI_6/MoO_3/**GO**	26.94	1.05	76.99	21.95	Sim	(Amjad et al., 2023)
AZO/SnO_2/$MAPbI_3$/Spiro OMeTAD/**RGO**	41.60	1.05	71.29	**31.26***	Sim	This work

5. Conclusion

This study has investigated the structural, morphological, and optical characteristics of the $MAPbI_3$ absorber. The $MAPbI_3$ film has a tetragonal structure, and the crystallites are preferentially oriented along the (110) with an average size of around 50 nm. The deposited PAL appears continuous and without porosity, with a thickness of 2.92 μm. The band gap (1.53 eV) and absorption coefficient ($5\times10^3 cm^{-1}$) of the $MAPbI_3$ absorber were extracted from the transmittance UV spectra, indicating a high absorption. Furthermore, based on experimental findings, a theoretical study of $MAPbI_3$-based planar PSC (i.e., ITO/SnO_2/$MAPbI_3$/Spiro-OMeTAD/Au) is conducted utilizing drift-diffusion SCAPS-1D simulations. The simulated PSC demonstrate a high efficiency of ~ 31.1% under real conditions. The simulations under real conditions include band-to-band coefficients, parasitic resistances (series and shunt), and reflections to understand their impact and the device physics. After considering all the real conditions, the cell's performance decreased from 31.1% to 22.55%. Then, the real conditions-based simulated device performance is improved by

optimizing the PAL thickness and N_t from 22.55% to 23.17%. The optimum PAL thickness range and N_t values are found to be at 2.3 μm to 4 μm and 3×10^{13} cm^{-3}, respectively. In addition, the back and the front contacts are varied to find the most effective solar cell structures, selecting RGO and AZO as effective alternatives to replace Au and ITO. The final solar cell efficiency is enhanced to 31.26%, which is closer to the Shockley-Queisser limit (33%).

In summary, this simulation results show that choosing suitable front and back electrodes efficiently helps to maximize the light absorption and minimize the recombination losses at interfaces. The combination of the experimental and the simulation studies advance the progress in $MAPbI_3$-based PSC development.

Acknowledgements

The authors would like to thank Marc Burgelman, University of Gent, Belgium, for providing free access to drift-diffusion SCAPS-1D simulation software.

References

Abderrezek, M., 2015. Modélisation des cellules solaires tandem à couches minces et à haut rendement. UNIVERSITE SETIF -1.

Amjad, A., Qamar, S., Zhao, C., Fatima, K., Sultan, M., Akhter, Z., 2023. Numerical simulation of lead-free vacancy ordered Cs2PtI6 based perovskite solar cell using SCAPS-1D. RSC Adv. 13, 23211–23222. https://doi.org/10.1039/D3RA04176J

Baloch, A.A.B., Hossain, M.I., Tabet, N., Alharbi, F.H., 2018. Practical Efficiency Limit of Methylammonium Lead Iodide Perovskite (CH3NH3PbI3) Solar Cells. J. Phys. Chem. Lett. 9, 426–434. https://doi.org/10.1021/acs.jpclett.7b03343

Barbé, J., Hughes, D., Wei, Z., Pockett, A., Lee, H.K.H., Heasman, K.C., Carnie, M.J., Watson, T.M., Tsoi, W.C., 2019. Radiation Hardness of Perovskite Solar Cells Based on Aluminum-Doped Zinc Oxide Electrode Under Proton Irradiation. Sol. RRL 3, 1900219. https://doi.org/10.1002/SOLR.201900219

Behrouznejad, F., Shahbazi, S., Taghavinia, N., Wu, H.P., Wei-Guang Diau, E., 2016. A study on utilizing different metals as the back contact of CH3NH3PbI3 perovskite solar cells. J. Mater. Chem. A 4, 13488–13498. https://doi.org/10.1039/c6ta05938d

Belaidi, I., Khelfaoui, F., Attaf, N., Azzizi, A., Aida, M.S., 2019. Solvent and Spinning Speed Effects on CH 3 NH 3 PbI 3 Films Deposited by Spin Coating 1900340, 1–9.

https://doi.org/10.1002/pssa.201900340

Burgelman, M., Nollet, P., Degrave, S., 2000. Modelling polycrystalline semiconductor solar cells. Thin Solid Films 361, 527–532. https://doi.org/10.1016/S0040-6090(99)00825-1

Burschka, J., Pellet, N., Moon, S.-J., Humphry-Baker, R., Gao, P., Nazeeruddin, M.K., Gratzel, M., 2013. Sequential deposition as a route to high-performance perovskite-sensitized solar cells. Nature 4–8. https://doi.org/10.1038/nature12340

Calió, L., Kazim, S., Grätzel, M., Ahmad, S., 2016. Hole-Transport Materials for Perovskite Solar Cells. Angew. Chemie - Int. Ed. 55, 14522–14545. https://doi.org/10.1002/anie.201601757

Cheng, Z., Lin, J., 2010. Layered organic – inorganic hybrid perovskites : structure , optical properties , film preparation , patterning and templating engineering. https://doi.org/10.1039/c001929a

Daboczi, M., Hamilton, I., Xu, S., Luke, J., Limbu, S., Lee, J., McLachlan, M.A., Lee, K., Durrant, J.R., Baikie, I.D., Kim, J.S., 2019. Origin of Open-Circuit Voltage Losses in Perovskite Solar Cells Investigated by Surface Photovoltage Measurement. ACS Appl. Mater. Interfaces 11, 46808–46817. https://doi.org/10.1021/acsami.9b16394

Dai, Z., Yadavalli, S.K., Hu, M., Chen, M., Zhou, Y., Padture, N.P., 2020. Effect of Grain Size on the Fracture Behavior of Organic-Inorganic Halide Perovskite Thin Films for Solar Cells. Scr. Mater. J. 185, 47–50. https://doi.org/10.1016/j.scriptamat.2020.03.044

Dang, Y., Zhou, Y., Liu, X., Ju, D., Xia, S., Xia, H., Tao, X., 2016. Formation of Hybrid Perovskite Tin Iodide Single Crystals by Top-Seeded Solution Growth. Angew. Chemie - Int. Ed. 55, 3447–3450. https://doi.org/10.1002/anie.201511792

Deepthi Jayan, K., Sebastian, V., 2021. Comprehensive device modelling and performance analysis of MASnI3 based perovskite solar cells with diverse ETM, HTM and back metal contacts. Sol. Energy 217, 40–48. https://doi.org/10.1016/j.solener.2021.01.058

Dou, B., Miller, E.M., Christians, J.A., Sanehira, E.M., Klein, T.R., Barnes, F.S., Shaheen, S.E., Garner, S.M., Ghosh, S., Mallick, A., Basak, D., Van Hest, M.F.A.M., 2017. High-performance flexible perovskite solar cells on ultrathin glass: Implications of the TCO. J. Phys. Chem. Lett. 8, 4960–4966. https://doi.org/10.1021/ACS.JPCLETT.7B02128/ASSET/IMAGES/LARGE/JZ-2017-02128M_0006.JPEG

Dunlop, E., Fabero, F., Friesen, G., Herrmann, W., Hohl-Ebinger, J., Mohring, H.-D., Mullejans, H., Virtuani, A., Warta, W., Zaaiman, W., Zamini, S., Taylor, N., 2010. Guidelines for PV Power Measurement in Industry.

Eperon, G.E., Burlakov, V.M., Docampo, P., Goriely, A., Snaith, H.J., 2014. Morphological Control for High Performance , Solution- Processed Planar Heterojunction Perovskite Solar Cells 151–157. https://doi.org/10.1002/adfm.201302090

Ford, W.E., Wessels, J.M., Rodgers, M.A.J., 1997. Electron injection by photoexcited Ru(bpy)32+ into colloidal SnO2: Analyses of the recombination kinetics based on electrochemical and Auger-capture models. J. Phys. Chem. B 101, 7435–7442. https://doi.org/10.1021/jp9700948

Garg, R., Dutta, N.K., Choudhury, N.R., 2014. Work function engineering of graphene. Nanomaterials 4, 267–300. https://doi.org/10.3390/nano4020267

Hao, F., Stoumpos, C.C., Chang, R.P.H., Kanatzidis, M.G., 2014. Anomalous band gap behavior in mixed Sn and Pb perovskites enables broadening of absorption spectrum in solar cells. J. Am. Chem. Soc. 136, 8094–8099. https://doi.org/10.1021/ja5033259

Hasnain, S.M., 2023. Examining the advances, obstacles, and achievements of tin-based perovskite solar cells: a review. Sol. Energy 262, 111825. https://doi.org/10.1016/j.solener.2023.111825

Hauck, M., Ligthart, T., Schaap, M., Boukris, E., Brouwer, D., 2017. Environmental benefits of reduced electricity use exceed impacts from lead use for perovskite based tandem solar cell. Renew. Energy 111, 906–913. https://doi.org/10.1016/j.renene.2017.04.044

Heo, J.H., Im, S.H., Noh, J.H., Mandal, T.N., Lim, C., Chang, J.A., Lee, Y.H., Kim, H., Sarkar, A., Nazeeruddin, K., Gra, M., 2013. Efficient inorganic–organic hybrid heterojunction solar cells containing perovskite compound and polymeric hole conductors. Nat. PHOTONICS | 1–6. https://doi.org/10.1038/NPHOTON.2013.80

Hossain, M.K., Toki, G.F.I., Alam, I., Pandey, R., Samajdar, D.P., Rahman, M.F., Islam, M.R., Rubel, M.H.K., Bencherif, H., Madan, J., Mohammed, M.K.A., 2023. Numerical simulation and optimization of a CsPbI3-based perovskite solar cell to enhance the power conversion efficiency. New J. Chem. 47, 4801–4817. https://doi.org/10.1039/d2nj06206b

Hosseini, S.R., Bahramgour, M., Yardani Sefidi, P., Tabatabaei Mashayekh, A., Moradi, A., Delibas, N., Hosseini, M.G., Niaei, A., 2022. Investigating the effect of non-ideal conditions on the performance of a planar CH3NH3PbI3-based perovskite solar cell through SCAPS-1D simulation. Heliyon 8. https://doi.org/10.1016/j.heliyon.2022.e11471

Im, J., Chun, J., Kim, S., Park, N., 2012. of a nanocrystalline 2H perovskite-type novel Synthesis , structure , and photovoltaic property of a nanocrystalline 2H perovskite-type novel. Nanoscale Res. Lett. 7, 353.

Im, J.H., Kim, H.S., Park, N.G., 2014. Morphology-photovoltaic property correlation in perovskite solar cells: One-step versus two-step deposition of CH3NH3PbI 3. APL Mater. 2. https://doi.org/10.1063/1.4891275

Isikgor, F.H., Zhumagali, S., Luis, L. V., De Bastiani, M., McCulloch, I., De Wolf, S., 2022. Molecular engineering of contact interfaces for high-performance perovskite solar cells. Nat. Rev. Mater. https://doi.org/10.1038/s41578-022-00503-3

Jiang, M., Zhang, W., Tang, J., 2022. Transient performance modelling of ultra-thin Sn-based perovskite solar cells based on electrode contact design to improve thermal stability. Eur. Phys. J. Plus 137. https://doi.org/10.1140/epjp/s13360-022-03174-9

Joo, Y.H., Um, D.S., Kim, C. Il, 2021. Tunable physical properties of Al-doped ZnO thin films by O2and Ar plasma treatments. Mater. Res. Express 8, 0–9. https://doi.org/10.1088/2053-1591/ac3f0a

Karimi, E., Ghorashi, S.M.B., 2017. Simulation of perovskite solar cell with P 3 HT hole-transporting materials . J. Nanophotonics 11, 032510. https://doi.org/10.1117/1.jnp.11.032510

Karthick, S., Velumani, S., Bouclé, J., 2020. Experimental and SCAPS simulated formamidinium perovskite solar cells: A comparison of device performance. Sol. Energy 205, 349–357. https://doi.org/10.1016/j.solener.2020.05.041

Kemp, K.W., Labelle, A.J., Thon, S.M., Ip, A.H., Kramer, I.J., Hoogland, S., Sargent, E.H., 2013. Interface recombination in depleted heterojunction photovoltaics based on colloidal quantum dots. Adv. Energy Mater. 3, 917–922. https://doi.org/10.1002/aenm.201201083

Khamkar, K.A., Bangale, S. V, Bamane, S.R., Dhapte, V. V, 2012. Preparation , Wettability properties of perovskite-type composite oxides nanocrystals by Combustion Route 4, 1522–1527.

Kim, H., Lee, C., Im, J., Lee, K., Moehl, T., Marchioro, A., Moon, S., Humphry-baker, R., Yum, J., Moser, J.E., Gra, M., 2012. All-Solid-State Submicron Thin Film 1–7. https://doi.org/10.1038/srep00591

Kojima, A., Teshima, K., Shirai, Y., Miyasaka, T., 2009. Organometal Halide Perovskites as Visible-Light Sensitizers for Photovoltaic Cells. https://doi.org/10.1021/ja809598r

La Ferrara, V., De Maria, A., Rametta, G., Della Noce, M., Mercaldo, L.V., Borriello, C., Bruno, A., Veneri, P.D., 2017. ZnO nanorods/AZO photoanode for perovskite solar cells fabricated in ambient air. Mater. Res. Express 4, 085025. https://doi.org/10.1088/2053-1591/aa7fcd

Lee, M.M., Teuscher, J., Miyasaka, T., Murakami, T.N., Snaith, H.J., 2012. Efficient Hybrid Solar

Cells Based on Meso-Superstructured Organometal Halide Perovskites. Sciencemag 10, 1–5.

Leijtens, T., Eperon, G.E., Barker, A.J., Grancini, G., Zhang, W., Ball, J.M., Kandada, A.R.S., Snaith, H.J., Petrozza, A., 2016. Carrier trapping and recombination: The role of defect physics in enhancing the open circuit voltage of metal halide perovskite solar cells. Energy Environ. Sci. 9, 3472–3481. https://doi.org/10.1039/c6ee01729k

Liang, Z., Zhang, S., Xu, X., Wang, N., Wang, J., Wang, X., Bi, Z., Xu, G., Yuan, N., Ding, J., 2015. A large grain size perovskite thin film with a dense structure for planar heterojunction solar cells via spray deposition under ambient conditions. RSC Adv. 5, 60562–60569. https://doi.org/10.1039/c5ra09110a

Liling, G.U.O., Zhang, S.U.N., Guanghui, Z., Xing, L.I., Hanxing, L.I.U., 2012. Synthesis and Characterization of Layered Perovskite-type 4, 957–961. https://doi.org/10.1007/s11595-012-0581-5

Lin H, Yang M, Ru X, Wang G, Yin S, Peng F, Hong C, Qu M, Lu J, Fang L, Han C, Procel P, Isabella O, Gao P, Li Z, Xu X, 2023. 26.7% Efficiency Silicon Heterojunction Solar Cells Achieved By Electrically Optimized Nanocrystalline-Silicon Hole Contact Layers. Nat. energy Artic. 14–16. https://doi.org/10.1038/s41560-023-01255-2

Loi, M.A., Hummelen, J.C., 2013. Perovskites under the Sun. Nat. Publ. Gr. 12, 1087–1089. https://doi.org/10.1038/nmat3815

Makableh, Y.F., C, I., Hassan, W., Aljaiuossi, G., 2020. Enhancement of the thermal properties of heterojunction perovskite solar cells by nanostructured contacts design. Sol. Energy 202, 204–209. https://doi.org/10.1016/j.solener.2020.04.002

Nakka, L., Cheng, Y., Aberle, A.G., Lin, F., 2022. Analytical Review of Spiro- OMeTAD Hole Transport Materials: Paths Toward Stable and Efficient Perovskite Solar Cells. Adv. Energy Sustain. Res. 3, 2200045. https://doi.org/10.1002/aesr.202200045

Name, C., Kumar, A., 2014. Perovskite Hybrid Solar Cell Reference. Cell 1–18.

Nh, C.H., Im, J., Chung, J., Kim, S., Park, N., 2012. Synthesis , structure , and photovoltaic property of a nanocrystalline 2H perovskite-type novel. Nanoscale Res. Lett. 7, 1. https://doi.org/10.1186/1556-276X-7-353

NREL, 2023. Best Research-Cell Efficiency Chart | Photovoltaic Research | NREL [WWW Document]. URL https://www.nrel.gov/pv/interactive-cell-efficiency.html

Pochont, N.R., Sekhar, Y.R., 2023. Numerical Simulation of Nitrogen-Doped Titanium Dioxide as an

Inorganic Hole Transport Layer in Mixed Halide Perovskite Structures Using SCAPS 1-D. Inorganics 11, 1–17. https://doi.org/10.3390/inorganics11010003

Qasim, I., Ahmad, O., Rashid, A., Farooq, M., Imran, M., Rashid, M., Hasnain, S.M., 2022. Design and numerical investigations of eco-friendly , non-toxic (Au / CuSCN / CH 3 NH 3 SnI 3 / CdTe / ZnO / ITO) perovskite solar cell and module. Sol. Energy 237, 52–61. https://doi.org/10.1016/j.solener.2022.02.056

Rahman, M.S., Miah, S., Marma, M.S.W., Sabrina, T., 2019. Simulation based Investigation of Inverted Planar Perovskite Solar Cell with All Metal Oxide Inorganic Transport Layers. 2nd Int. Conf. Electr. Comput. Commun. Eng. ECCE 2019. https://doi.org/10.1109/ECACE.2019.8679283

Rawat, S., Shrivastav, N., Madan, J., 2023a. Analysis and Optimization of MASnPbI3-based Single Junction Solar Cells for High Power Conversion Efficiency. 2023 2nd Int. Conf. Electr. Electron. Inf. Commun. Technol. ICEEICT 2023 1–3. https://doi.org/10.1109/ICEEICT56924.2023.10157594

Rawat, S., Shrivastav, N., Pandey, R., Madan, J., 2023b. Optimizing Photovoltaic Performance of MASnPbI3 Perovskite Solar Cells through Layer Thickness Variations. Proc. 5th Int. Conf. 2023 Devices Integr. Circuit 38–41. https://doi.org/10.1109/DevIC57758.2023.10134949

Rawat, S., Shrivastav, N., Pandey, R., Madan, J., 2023c. Optimizing Photovoltaic Performance of MASnPbI3 Perovskite Solar Cells through Layer Thickness Variations. Proc. 5th Int. Conf. 2023 Devices Integr. Circuit, DevIC 2023 38–41. https://doi.org/10.1109/DEVIC57758.2023.10134949

Reyes, A.C.P., Lázaro, R.C.A., Leyva, K.M., López, J.A.L., Méndez, J.F., Jiménez, A.H.H., Zurita, A.L.M., Carrillo, F.S., Durán, E.O., 2021. Study of a lead-free perovskite solar cell using CZTS as HTL to achieve a 20% PCE by SCAPS-1D simulation. Micromachines 12. https://doi.org/10.3390/mi12121508

Rousseau, J., Gibaud, A., 2006. CRISTALLOGRAPHIE GÉOMÉTRIQUE et RADIOCRISTALLOGRAPHIE, 3eme ed.

Rutledge, S.A., Helmy, A.S., 2013. Carrier mobility enhancement in poly(3,4-ethylenedioxythiophene)- poly(styrenesulfonate) having undergone rapid thermal annealing. J. Appl. Phys. 114. https://doi.org/10.1063/1.4824104

Safie, N.E., Sairi, M.N.F.M., Azam, M.A., Takasaki, A., 2022. Development and analysis of rGO-MoS2 nanocomposite as top electrode for the application of inverted planar perovskite solar cells

via SCAPS-1D device simulation. J. Mater. Res. 37, 3372–3383. https://doi.org/10.1557/S43578-022-00652-9/FIGURES/8

Schulz, P., Cahen, D., Kahn, A., 2019. Halide Perovskites: Is It All about the Interfaces? Chem. Rev. 119, 3349–3417. https://doi.org/10.1021/acs.chemrev.8b00558

Schulz, P., Edri, E., Kirmayer, S., Hodes, G., Cahen, D., Kahn, A., 2014. Interface energetics in organo-metal halide perovskite-based photovoltaic cells. Energy Environ. Sci. 7, 1377–1381. https://doi.org/10.1039/c4ee00168k

Sekar, K., Nakar, R., Bouclé, J., Doineau, R., Nadaud, K., Schmaltz, B., Poulin-Vittrant, G., 2022. Low-Temperature Hydrothermal Growth of ZnO Nanowires on AZO Substrates for FACsPb(IBr)3 Perovskite Solar Cells. Nanomaterials 12, 2093. https://doi.org/10.3390/nano12122093

Serhan, M., Sprowls, M., Jackemeyer, D., Long, M., Perez, I.D., Maret, W., Tao, N., Forzani, E., 2019. Interface Engineering for High-Performance Perovskite Hybrid Solar Cells. AIChE Annu. Meet. Conf. Proc. 2019-Novem. https://doi.org/10.1039/x0xx00000x

Sha, W.E.I., Ren, X., Chen, L., Choy, W.C.H., 2015. The efficiency limit of CH3NH3PbI3 perovskite solar cells. Appl. Phys. Lett. 106. https://doi.org/10.1063/1.4922150

Shaikh, J.S., Shaikh, N.S., Sheikh, A.D., Mali, S.S., Kale, A.J., Kanjanaboos, P., Hong, C.K., Kim, J.H., Patil, P.S., 2017. Perovskite solar cells: In pursuit of efficiency and stability. Mater. Des. 136, 54–80. https://doi.org/10.1016/j.matdes.2017.09.037

Shockley, W., Queisser, H.J., 1961. Detailed balance limit of efficiency of p-n junction solar cells. J. Appl. Phys. 32, 510–519. https://doi.org/10.1063/1.1736034

Shyma, A.P., Sellappan, R., 2022. Computational Probing of Tin-Based Lead-Free Perovskite Solar Cells : Effects of Absorber Parameters and Various. Materials (Basel). 15.

Sibin, K.P., Swain, N., Chowdhury, P., Dey, A., Sridhara, N., Shashikala, H.D., Sharma, A.K., Barshilia, H.C., 2016. Optical and electrical properties of ITO thin films sputtered on flexible FEP substrate as passive thermal control system for space applications. Sol. Energy Mater. Sol. Cells 145, 314–322. https://doi.org/10.1016/j.solmat.2015.10.035

Takahashi, Yukari, Obara, R., Lin, Z., Takahashi, Yukihiro, 2011. Charge-transport in tin-iodide perovskite CH3NH3SnI3 : origin of high conductivity Takahashi. Dalt. Trans. 40, 5563–5568. https://doi.org/10.1039/c0dt01601b.1

Tidhar, Y., Edri, E., Weissman, H., Zohar, D., Hodes, G., Cahen, D., Rybtchinski, B., Kirmayer, S.,

2014. Crystallization of Methyl Ammonium Lead Halide Perovskites: Implications for Photovoltaic Applications. J. Am. Chem. Soc. 136, 13249−13256. https://doi.org/10.1021/ja505556s

Wang, W., Liu, R., Dong, C., Xie, Y., Jiang, M., Dong, G., Zhou, H., 2023. Wet-chemical surface texturing of AZO substrate for improved perovskite solar cells. J. Alloys Compd. 963, 171105. https://doi.org/10.1016/J.JALLCOM.2023.171105

Yang, B., Bogachuk, D., Suo, J., Wagner, L., Kim, H., Lim, J., Hinsch, A., Boschloo, G., Nazeeruddin, M.K., Hagfeldt, A., 2022. Strain effects on halide perovskite solar cells. Chem. Soc. Rev. https://doi.org/10.1039/d2cs00278g

Yuan, J., Hazarika, A., Zhao, Q., Ling, X., Moot, T., Ma, W., Luther, J.M., 2020. Metal Halide Perovskites in Quantum Dot Solar Cells: Progress and Prospects. Joule 4, 1160–1185. https://doi.org/10.1016/j.joule.2020.04.006

Zandi, S., Razaghi, M., 2019. Finite element simulation of perovskite solar cell: A study on efficiency improvement based on structural and material modification. Sol. Energy 179, 298–306. https://doi.org/10.1016/j.solener.2018.12.032

Zhang, C., Liang, S., Liu, W., Eickemeyer, F.T., Cai, X., Zhou, K., Bian, J., Zhu, H., Zhu, C., Wang, N., Wang, Z., Zhang, J., Wang, Y., Hu, J., Ma, H., Xin, C., Zakeeruddin, S.M., Grätzel, M., Shi, Y., 2021. Ti1−graphene single-atom material for improved energy level alignment in perovskite solar cells. Nat. Energy 2021 612 6, 1154–1163. https://doi.org/10.1038/s41560-021-00944-0

Zhang, W., Saliba, M., Moore, D.T., Pathak, S.K., Hörantner, M.T., Stergiopoulos, T., Stranks, S.D., Eperon, G.E., Alexander-Webber, J.A., Abate, A., Sadhanala, A., Yao, S., Chen, Y., Friend, R.H., Estroff, L.A., Wiesner, U., Snaith, H.J., 2015. Ultrasmooth organic-inorganic perovskite thin-film formation and crystallization for efficient planar heterojunction solar cells. Nat. Commun. 6. https://doi.org/10.1038/ncomms7142

Zhao, Y., Ma, F., Qu, Z., Yu, S., Shen, T., Deng, H.X., Chu, X., Peng, X., Yuan, Y., Zhang, X., You, J., 2022. Inactive (PbI2)2RbCl stabilizes perovskite films for efficient solar cells. Science (80-.). 377, 531–534. https://doi.org/10.1126/science.abp8873

Zhou, H., Chen, Q., Li, Luo, S., Tze-bing Song, Hsin-Sheng Duan, Z.H., Jingbi You, Yongsheng Liu, Y.Y., 2014. Interface engineering of highly efficient perovskite solar cells. sciencemag 345. https://doi.org/10.1126/science.1254050

Highlights

- Exploring of the structural, morphological, and optical characteristics of the $MAPbI_3$ absorber layer to obtain a deeper understanding of its essential characteristics, which serve for theatrical study.
- Theatrical study through SCAPS-1D of ITO/SnO_2/$MAPbI_3$/Spiro-OMeTAD/Au n-i-p planar structure based on experimental investigation results.
- Achieved remarkable performance in $MAPbI_3$ PSCs by optimizing the front contact and enhancing light absorption while reducing recombination losses.
- The study reports a noteworthy solar cell efficiency of 31.26%, representing a significant step forward in the development of high-efficiency solar energy devices.

Graphical Abstract